

Competing forces in liquid metal electrodes and batteries

Ashour, R.; Kelley, D.; Salas, A.; Starace, M.; Weber, N.; Weier, T.;

Originally published:

February 2018

Journal of Power Sources 378(2018), 301-310

DOI: <https://doi.org/10.1016/j.jpowsour.2017.12.042>

Perma-Link to Publication Repository of HZDR:

<https://www.hzdr.de/publications/Publ-26193>

Release of the secondary publication
on the basis of the German Copyright Law § 38 Section 4.

CC BY-NC-ND

Competing forces in liquid metal electrodes and batteries

Rakan F. Ashour^a, Douglas H. Kelley^a, Alejandro Salas^{b,c}, Marco Starace^b,
Norbert Weber^b, Tom Weier^b

^a*University of Rochester, 235 Hopeman Building, Rochester, NY 14627, USA*

^b*Helmholtz-Zentrum Dresden – Rossendorf, Bautzner Landstr. 400, Dresden, Germany*

^c*Instituto Tecnológico y de Estudios Superiores de Monterrey, Monterrey, Mexico*

Abstract

Liquid metal batteries have been proposed for low-cost grid scale energy storage. During their operation, solid intermetallic phases often form in the cathode and are known to limit the efficiency of the cell. Fluid flow in the liquid electrodes can enhance mass transfer and reduce or avoid the formation of intermetallics, and fluid flow can be promoted by careful choice of the locations and topology of a battery's electrical connections, which affect the thermal buoyant forces and electromagnetic forces acting on the electrodes. In this context we study four phenomena that drive flow: Rayleigh-Bénard convection, internally heated convection, electro-vortex flow, and swirl flow, in both experiment and simulation. In experiments, we use ultrasound Doppler velocimetry (UDV) to measure the flow of an electrode made of liquid eutectic PbBi at 160 °C and subject to all four phenomena. In numerical simulations, we isolate the phenomena and simulate each separately using OpenFOAM. Comparing simulated velocities to experiments via a UDV beam model, we find that all four phenomena can enhance mass transfer in LMBs. We explain the flow direction and structure, and give estimates for the magnitude of the mean velocity depending on the cell current. We describe how the phenomena interact and propose dimensionless numbers for estimating their mutual relevance. A brief discussion of electrical connections summarizes the engineering implications of our work.

Keywords: liquid metal battery, electro-vortex flow, internally heated convection, swirl flow, Rayleigh-Bénard convection

1. Introduction

Electrical grids work by balancing the level of demand and supply. Today, the fluctuations are typically handled by gas-fired turbines, which are turned on during the peak demand of electricity. The electrical grid must be designed for that peak power since it lacks an efficient storage mechanism to dampen the load. The increasing integration of renewable energy sources will likely cause even higher fluctuations that cannot be handled by the grid in its current state [1, 2]. Large scale stationary energy storage would likely become mandatory to compensate the fluctuations. Due to its low price, the liquid metal battery (LMB) might be an ideal storage technology [3, 4].

An LMB is composed of two liquid metals with different electronegativity separated by a layer of molten salt electrolyte (Fig. 1a). Typical chemistries include Ca||Bi [5, 6], Ca||Sb [7, 8], K||Hg [9], Li||Bi [10, 11], Li||Cd [12], Li||Pb [4, 12], Li||Sb [4], Li||Se [13, 14], Li||Sn [15, 16], Li||Te [17], Li||Zn [12], Mg||Sb [18], Na||Bi [19, 20], Na||Hg [21, 22], Na||Pb [12], Na||Sb [3], Na||Sn [9, 23, 24], Na||Zn [25, 26] and Zn||Bi,Sn,Pb [27, 28] cells. The three liquid layers are self-segregated based on density, which makes the manufacturing process simpler and less expensive compared to other batteries. We will consider LMBs of cylindrical shape, though rectangular shapes are also possible. When the battery is connected to an external load, alkali or alkaline metal ions (A^+) are produced via oxidation. These metal ions have to travel through the molten electrolyte before they are reduced at the surface of the positive electrode (B) where they form an alloy $A_{in\ B}$. The open circuit potential of the battery depends on the Gibbs free energy of the alloying reaction [3]. The all-liquid design allows for fast charge transfer kinetics [29] and current densities up to 13 A/cm^2 [12–14]. At low currents, the ohmic losses in the electrolyte layer are the most important overpotential. However, at higher current densities concentration polarization becomes the main challenge [9, 21, 24, 30]; due to the slow diffusion of reaction products [3, 18], intermetallic phases are formed at the cathode-electrolyte interface [12, 31]. Often they float on top of the cathode metal because of their low density [8], and sometimes dendrites may even short-circuit the cell [5]. The solid intermetallic layer will not only hamper mass transfer, but will also act as a solid wall slowing down the flow in the cell. A local accumulation of intermetallic phases will lead to a modified conductivity distribution, causing small scale electro-vortex flow. Hence, a gentle mixing of the bottom electrode may crucially increase cell performance.

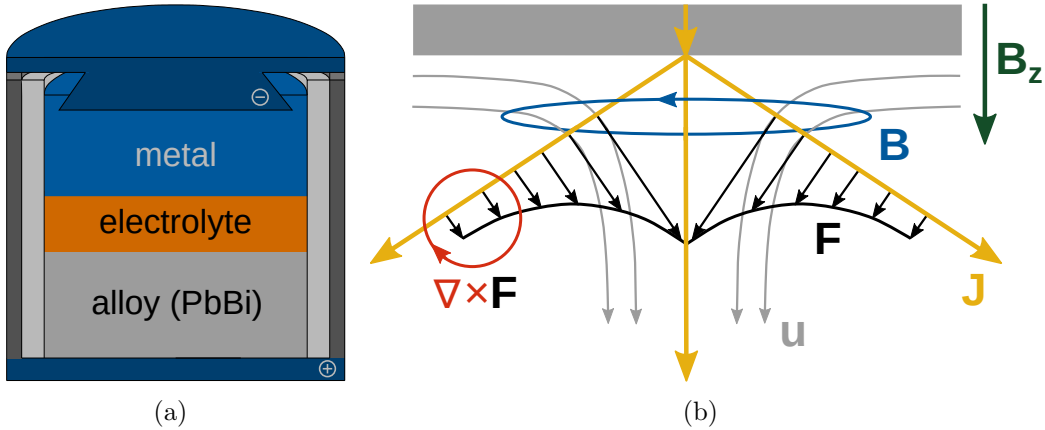


Figure 1: Sketch of a typical liquid metal battery, which is cylindrical and shown in cross-section (a), and electro-vortex flow at a point current source (b: adapted from [32]). Diverging current produces a force with nonzero curl that necessarily drives flow, and current always diverges from the negative current collector of a liquid metal battery.

38 Fluid flow in individual cells does not only affect the cell’s efficiency.
 39 Perhaps more importantly, the development of fast flows imposes a risk of
 40 interface deformations that can lead to an electrical short and sudden dis-
 41 charge of the cell. Prior work in that context focused on the Taylor instability
 42 (TI) [33–40], which will appear first in the top electrode. The TI may be
 43 suppressed by different means [33, 36] and is likely to short-circuit only very
 44 large cells (with a diameter on the order of meters) [37]. In contrast, magne-
 45 tohydrodynamic (MHD) instabilities of the metal-electrolyte interfaces may
 46 appear in small cells, too. Well known from aluminum reduction cells, this
 47 “sloshing” or “metal pad roll” instability can be explained by the interaction
 48 of horizontal currents with a magnetic background field [41–44]. Small den-
 49 sity differences between metal and electrolyte and strong vertical magnetic
 50 fields promote this instability [44, 45]. In LMBs, the two liquid interfaces can
 51 influence each other and may lead to very complex coupling [46, 47] which
 52 is still under investigation. Further, thermal convection (TC) is expected
 53 to appear especially in the electrolyte and upper metal layer. Although TC
 54 will be present in very small cells, its (moderate) flow will not endanger the
 55 safe operation of small and medium sized LMBs [48]. Marangoni convection
 56 driven by a surface tension gradient is not expected to influence the flow ve-
 57 locity considerably, but is expected to change the size of the Rayleigh-Bénard
 58 cells [49]. Finally, TC was also found to enhance mass transfer in the positive

59 electrode [50, 51], e.g. by heating the cell from below. For a discussion of
60 the thermal balance of an LMB, see [52].

61 Electro-vortex flow (EVF) can also drive flow in LMBs. Its usefulness
62 for mixing LMBs and its implications for the safe operation of LMBs were
63 already discussed in [53, 54] and [55]. The origin of EVF is best explained
64 by the illustrative example of Shercliff [32] (Fig. 1b). An electric current
65 density J passes from a point source into an infinite fluid layer. Within the
66 fluid, the current diverges radially. The resulting Lorentz force F (which
67 is the cross product of the current density with its own magnetic field B)
68 is non-conservative, i.e. its curl does not vanish. It can therefore not be
69 balanced by a pressure gradient and drives a flow \mathbf{u} away from the wall.
70 This phenomenon is commonly denoted as “electrically driven vortical flow”
71 or shorter “electro-vortex flow”. The term “vortex” refers to the typical
72 flow structure observed in confined volumes. EVF is caused by *internal*
73 currents producing a *rotational* Lorentz force and driving a jet away from
74 the wall [32]. It cannot exist in 2D [32]. Since battery electrodes are typically
75 wider than the wires that supply their currents, and current collectors must
76 be made small enough to prevent shorts with vessel walls, battery currents
77 almost always diverge, at least in some regions of the electrode. The extent
78 to which they diverge and drive electro-vortex flow depends on connection
79 topology.

80 Already one year before Shercliff, Lundquist studied the same problem.
81 He discovered that the velocity of EVF scales with the so-called EVF pa-
82 rameter $S = \mu_0 I^2 / (4\pi^2 \rho \nu^2)$ [56, 57] with μ_0 , I , ρ and ν denoting the vacuum
83 permeability, the current, the density, and the kinematic viscosity, respec-
84 tively (for different definitions, see [58, 59]; [59] might have a typo). At
85 typical currents for industrial applications the velocity scales as $u \sim \sqrt{S}$,
86 i.e. linearly with the current. Only at low currents, a quadratic scaling is
87 observed [57, 59, 60]. It should be further noted that the jet is steady only
88 at very low velocities; typically, it oscillates (see e.g., [61, 62]). At the veloc-
89 ity increases, dissipative mechanisms strengthen and the velocity no longer
90 scales linearly with current; the flow saturates. At low velocities, the main
91 dissipative mechanisms are often induced current or magnetic field (as, e.g.,
92 the Tayler instability [39, 40]). However, at typical velocities, the main dis-
93 sipation happens in the boundary layers because of viscosity [61, 63] (for an
94 experimental study see [64]). The thoroughly studied problem of an infinite
95 fluid layer [56, 58, 65–71] (overview [57, 72]) is therefore of limited practical
96 relevance because it involves no boundary layers.

97 Davidson provides a concise, clear, and understandable introduction to
98 electro-vortex flow [61]. For an even shorter introduction, see Chudnovskii
99 [73] and for a broad overview on EVF and its application Bojarevics et al.
100 [60]. A number of experiments on electro-vortex were conducted by Woods
101 et al. [74], Butsenieks et al. [59, 75–77], Bojarevics et al. [78], Zhilin et al.
102 [43, 64, 79] and Rübiger et al. [80–82]; for an excellent overview, see [60].

103 At low currents the jet illustrated in Fig. 1b usually forms a poloidal
104 flow that descends along the axis of the cylindrical electrode and rises along
105 the walls, since it is confined by boundaries. However, at high currents an
106 azimuthal flow or “spontaneous swirl” [61] is often observed experimentally
107 [74, 83]. Its origin can be explain similar to the Sele mechanism in alu-
108 minium reduction cells [41, 44]. A vertical magnetic background field and
109 the radial cell current produce an azimuthal force driving an azimuthal flow.
110 The background magnetic field may be the Earth’s magnetic field [83]; simi-
111 larly a “slight deviation from symmetry” in the experiment will lead to swirl
112 [62, 63, 78]. Making electrical connections among a tightly-packed array of
113 batteries is almost certain to cause such deviations from symmetry. The spin-
114 up takes a significant time (around a minute in large vacuum arc remelting
115 vessels) [84]; therefore, swirling may be minimized by periodically reversing
116 the direction of the vertical background field [84].

117 Curiously, the swirl is known to almost totally supersede the poloidal
118 flow. Davidson explains that “the radial stratification of angular momentum
119 suppresses radial motion in the same way as density stratification suppresses
120 axial motion” [84]. He demonstrates that the azimuthal flow suppresses the
121 poloidal one (“poloidal suppression”) and argues that Ekman pumping [85]
122 is the key dissipative mechanism [63]. He further predicts that an azimuthal
123 force of only 1% of the poloidal one will lead to a strong swirl flow. Alternate
124 explanations have also been proposed, however [76, 83, 86].

125 In this article we study the flow in the bottom electrode only. Specifically
126 we investigate the interaction of four different flow phenomena: electro-vortex
127 flow, swirl flow, internally heated convection (IHC) and classical Rayleigh-
128 Bénard convection. All four depend strongly on the location and topology
129 of electrical connections to the battery. Those connections are likely to be
130 tightly packed into a large array of batteries, since the technology is intended
131 to store enough energy for neighborhoods or cities. Where the connections
132 enter and leave each battery, how much they concentrate the electrical cur-
133 rent, and what paths they take outside the batteries can all affect flow in the
134 electrode. To study the effects of connection on the four flow phenomena, we

135 use a combination of experimental and numerical models of PbBi electrodes
136 operating at mean current densities of up to 0.65 A/cm^2 .

137 The paper proceeds as follows: in the next section we describe the exper-
138 imental apparatus and numerical model, followed by an order of magnitude
139 estimation of the different flows in section 3. Finally we present and discuss
140 the results in section 4.

141 2. Methods

142 2.1. Experimental

143 A schematic of the experimental apparatus is shown in Fig. 2. The vessel
144 is a cylinder of 304 stainless steel with inner radius $R = 44.5 \text{ mm}$ that also
145 serves as the positive current collector. The liquid metal used in the experi-
146 ments is a eutectic alloy of 44.5% lead and 55.5% bismuth. The vessel rests
147 on an aluminum plate which is much more conductive than stainless steel,
148 thereby allowing heat and current density to homogenize before entering the
149 vessel. The upper current collector is a 4 mm-diameter nickel-plated copper
150 wire with mica and fiberglass insulation. It is mounted on a PTFE sheet
151 using shaft collars and is connected to a current-controlled DC power source.
152 Two K-type thermocouples are placed at different depths to measure the tem-
153 perature difference between the top and bottom of the liquid metal electrode.
154 A third thermocouple is connected to a proportional-integral-derivative con-
155 troller, which allows for the temperature to be maintained at $160 \text{ }^\circ\text{C}$ (at the
156 bottom of the cell). The temperature is chosen to match the operating con-
157 ditions of a Na||PbBi battery [87]. The apparatus minimizes heat exchange
158 by using ceramic insulation, which allows for the operating temperature to
159 be maintained for the duration of the experiment [see 50, 88].

160 Since liquid metal is opaque, it is not possible to measure flow using op-
161 tical methods like particle tracking or particle image velocimetry. Therefore,
162 to study mixing and transport in liquid metal electrodes we use an ultra-
163 sound Doppler velocimeter (Signal-Processing DOP 3010). The velocimeter
164 drives an ultrasound probe that makes a beep and listens for echoes. The
165 distance of an echoing body is determined from the speed of sound and the
166 time delay between emitted and received signals. The speed of that body
167 toward or away from the probe is determined from the Doppler shift of the
168 echo. Negative values in the velocity profile indicate a flow moving toward
169 the probe, whereas positive values indicate a flow away from the probe. Small
170 oxide particles or other impurities common in liquid metal provide sufficient

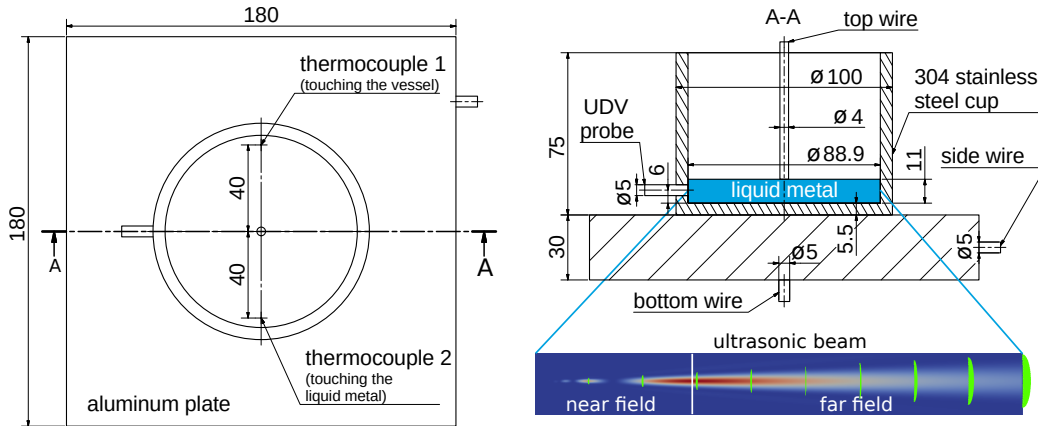


Figure 2: Dimensions of the experiment and simulation model (in mm) and illustration of the ultrasound beam showing the near and far field as well as the beam broadening.

171 echoes. The probe operates with a frequency of 8 MHz and has a piezoelectric
 172 emitter of diameter 5 mm, which gives a radial resolution of 0.5 mm and lat-
 173 eral resolution of a few mm. In the apparatus shown in Fig. 2, the ultrasound
 174 probe is mounted on the side of the cylinder allowing for the measurement of
 175 the radial velocity component of the flow along a diameter, 6 mm above the
 176 vessel floor. The cylinder is filled with 700 g of eutectic PbBi, which gives
 177 a realistic electrode thickness of about 11 mm. Though UDV measurements
 178 in similar shallow layers were already successfully conducted in the past [89],
 179 our experiment is fairly challenging. As the UDV beam broadens on its way
 180 (Fig. 2), it samples flow in a finite volume in which the velocity is not neces-
 181 sarily uniform; regions of flow towards and away from the probe may cancel
 182 each other out. In order to correctly compare the simulated velocities, we
 183 use a simple UDV beam model (Appendix A).

184 To study the effect of electric current topology on fluid flow, two different
 185 current paths are investigated. In one arrangement, current is supplied to
 186 the side of the aluminum plate. This model is very likely to be seen in
 187 battery packs (see e.g., Fig. 20 in [53, 54]). In the other arrangement,
 188 current is supplied to the bottom of the aluminum plate through a 100 cm
 189 long aluminum rod. This arrangement represents vertically stacked cells and
 190 minimizes symmetry-breaking in the supply currents, thereby reducing swirl
 191 flow.

192 *2.2. Mathematical and numerical model*

193 In our simulations, thermal convection and electro-vortex flow are mod-
 194 eled separately. The two models are implemented in the open source li-
 195 brary OpenFOAM [90]. If not otherwise stated, the following material prop-
 196 erties are assumed for eutectic PbBi at 160 °C: a kinematic viscosity of
 197 $\nu = 2.7 \cdot 10^{-7} \text{ m}^2/\text{s}$, a volumetric thermal expansion coefficient of $\beta =$
 198 $1.3 \cdot 10^{-4} \text{ K}^{-1}$, an electric conductivity of $\sigma = 9 \cdot 10^5 \text{ S/m}$, a density of
 199 $\rho = 10505 \text{ kg/m}^3$, an isobaric heat capacity of $c_p = 148 \text{ J/kg/K}$, a heat
 200 conductivity of $\lambda = 10 \text{ W/m/K}$, a thermal diffusivity $\alpha = 6 \cdot 10^{-6} \text{ m}^2/\text{s}$, a
 201 Prandtl number of $Pr = 0.04$ and a sound velocity of $c = 1765 \text{ m/s}$ [91–93].
 202 The electric conductivity of the vessel is assumed to be $\sigma = 1.37 \cdot 10^6 \text{ S/m}$
 203 and that of the aluminum plate $\sigma = 3.5 \cdot 10^7 \text{ S/m}$.

204 *2.2.1. Thermal convection*

205 Thermal effects are modeled in the fluid only. All solid conductors are
 206 replaced by simplified boundary conditions. The flow is simulated using the
 207 Oberbeck-Boussinesq approximation [94]. Its validity is estimated according
 208 to Gray and Giorgini [95]: a temperature difference of 27 K would lead to
 209 an error of 10 % of the dynamic viscosity, when neglecting its temperature
 210 dependence. Respectively, the temperature difference may reach 66 K for
 211 thermal conductivity and 833 K for c_p and density in order to stay below the
 212 same error. As we expect temperature differences in the order of 10 K, the
 213 Oberbeck approximation is well-suited for our problem. The Navier-Stokes
 214 and energy equations

$$\frac{\partial \mathbf{u}}{\partial t} + \nabla \cdot (\mathbf{u}\mathbf{u}) = -\nabla p_d + \nu \Delta \mathbf{u} - \mathbf{g} \cdot \mathbf{r} \nabla \rho_k \quad (1)$$

$$\nabla \cdot \mathbf{u} = 0 \quad (2)$$

$$\frac{\partial T}{\partial t} + \nabla \cdot (\mathbf{u}T) = \frac{\lambda}{\rho_0 c_p} \Delta T + \frac{\mathbf{J}^2}{\sigma \rho_0 c_p} \quad (3)$$

215 are solved, with \mathbf{u} , t , \mathbf{g} , \mathbf{r} , T , and \mathbf{J} denoting velocity, time, gravitational
 216 acceleration, position, temperature, and current density, respectively. The
 217 density $\rho = \rho_0 \rho_k = \rho_0 (1 - \beta(T - T_{\text{ref}}))$ is calculated using the mean density
 218 ρ_0 at reference temperature T_{ref} and the coefficient of thermal expansion β .
 219 The current density is computed with the electro-vortex solver and provided
 220 as initial condition. The modified pressure is defined as $p_d = (p - \rho \mathbf{g} \cdot \mathbf{r})/\rho_0$,
 221 where p is the pressure. The set of equations is solved using the PISO algo-
 222 rithm on a collocated grid (with Rhie-Chow interpolation [96]) employing a

223 modified version of the OpenFOAM standard solver *buoyantBoussinesqPimpleFoam*
 224 and using at least 300 cells on the diameter.

225 2.2.2. Electro-vortex flow

226 Simulating electro-vortex flow requires the coupling of solid and liquid
 227 conductors to obtain the correct current density. This coupling is achieved
 228 by a parent-child mesh technique. While electric properties (electric poten-
 229 tial, current density) are solved on a global mesh, the flow is computed in the
 230 fluid region only, so quantities must be mapped between meshes. The mag-
 231 netic field is determined by an integro-differential approach, i.e. its boundary
 232 conditions are computed using Biot-Savart’s integral [35] and the induction
 233 equation is solved in the fluid. The model is described in detail in [97].

234 The electric potential Φ , current density \mathbf{J} and magnetic field \mathbf{B} are split
 235 into constant (subscript 0) and induced parts (lower case) as

$$\Phi = \Phi_0 + \varphi \quad (4)$$

$$\mathbf{J} = \mathbf{J}_0 + \mathbf{j} \quad (5)$$

$$\mathbf{B} = \mathbf{B}_0 + \mathbf{b}. \quad (6)$$

236 The induced magnetic field \mathbf{b} is neglected. The following set of equations is
 237 solved on the global mesh:

$$\nabla \cdot \sigma \nabla \Phi_0 = 0 \quad (7)$$

$$\nabla \cdot \sigma \nabla \varphi = \nabla \cdot \sigma (\mathbf{u} \times \mathbf{B}) \quad (8)$$

$$\mathbf{J}_0 = -\sigma \nabla \Phi_0 \quad (9)$$

$$\mathbf{j} = \sigma (-\nabla \varphi + \mathbf{u} \times \mathbf{B}). \quad (10)$$

238 In the fluid region we solve

$$\frac{\partial \mathbf{u}}{\partial t} + (\mathbf{u} \cdot \nabla) \mathbf{u} = -\nabla p + \nu \Delta \mathbf{u} + \frac{\mathbf{J} \times \mathbf{B}}{\rho} \quad (11)$$

$$\mathbf{B}_0(\mathbf{r}) = \frac{\mu_0}{4\pi} \int \frac{\mathbf{J}_0(\mathbf{r}') \times (\mathbf{r} - \mathbf{r}')}{|\mathbf{r} - \mathbf{r}'|^3} dV' \quad (12)$$

$$0 = \Delta \mathbf{B}_0 \quad (13)$$

239 with μ_0 and V denoting the vacuum permeability and cell volume, respec-
 240 tively. Computing Biot-Savart’s integral, the current \mathbf{J} of the full mesh is
 241 used for determining \mathbf{B} at the fluid boundaries only. The grid resolution
 242 is approximately 100 cells on the diameter with strongly refined boundary
 243 layers.

244 **3. Theory of transport in liquid metal electrodes**

245 In this section, we will derive two simple dimensionless numbers for esti-
 246 mating which flow dominates: thermal convection or electro-vortex flow. We
 247 will start with classical Rayleigh-Bénard convection.

248 A typical liquid metal battery setup requires heating a cylindrical con-
 249 tainer from the bottom, which generates a temperature gradient along the
 250 depth of the electrode. As the liquid closer to the bottom becomes less dense,
 251 it rises to the surface allowing for the cooler fluid to sink down. A steady
 252 flow is established when the balance of kinetic energy and viscous dissipation
 253 is reached. In systems where the viscosity is high enough, or length scales
 254 are small enough, fluid motion can be completely suppressed. The onset
 255 of thermal convection is defined by the Rayleigh number (i.e. the ratio of
 256 buoyant to viscous forces) as

$$Ra = \frac{g\beta h^3(T - T_0)}{\alpha\nu}, \quad (14)$$

257 with g , h , and $T - T_0$ denoting the gravitational acceleration, the height of
 258 the layer, and the temperature difference, respectively, all at working tem-
 259 perature $T_0 = 160$ °C. In our specific experiment with a free upper surface,
 260 convection is expected to set in at a critical Rayleigh number of $Ra_{cr} = 1100$
 261 [98], which corresponds to a temperature difference of $\Delta T \approx 1$ K. We expect
 262 therefore strong Rayleigh-Bénard convection in the experiment, which we
 263 maintain at a temperature difference of $\Delta T \approx 8$ K. The typical velocity scale
 264 of Rayleigh-Bénard convection can be estimated by the free fall velocity as
 265 [48, 99]

$$U_b \sim \sqrt{g\beta\Delta Th}. \quad (15)$$

266 We will now proceed with the case of internally heated convection (IHC),
 267 which is caused by Joule heating of the electric current due to ohmic losses.
 268 Similarly, the free fall velocity may be used as velocity scale. However, some
 269 characteristic temperature difference needs to be defined first. Following
 270 Goluskin [48, 100] we can use the heating rate $\dot{Q}' = J^2/(\sigma\rho c_p)$ [101] to
 271 obtain a characteristic temperature gradient

$$\Delta T = \frac{h^2 J^2}{\alpha\sigma\rho c_p}. \quad (16)$$

272 Finally, we consider electro-vortex flow. When an electrical current den-
 273 sity \mathbf{J} is injected into the fluid, it induces a magnetic field \mathbf{B} , and the two
 274 are related via Ampere's law as

$$\oint_C \mathbf{B} d\ell = \mu_0 \int_S \mathbf{J} dS, \quad (17)$$

275 with S , C and $d\ell$ denoting a surface, the curve around the surface and an
 276 infinitesimal element of the curve. In geometries relevant for liquid metal bat-
 277 teries, electrical current flows between two current collectors, both aligned
 278 on the axis of symmetry. Typically, the upper current collector has a smaller
 279 diameter than the lower one. Given that geometry, we first consider purely
 280 axial current, which would drive a circulation that rises near the side walls
 281 and descends near the center. To see why, apply (17) to two paths of integra-
 282 tion, both circles of the same radius and both aligned with the central axis,
 283 but at different heights. Since current is more concentrated near the smaller,
 284 upper current collector, the magnetic field there is larger. The Lorentz force
 285 points toward the central axis everywhere; however, it has larger magnitude
 286 near the upper current collector, causing an inward flow there. Conservation
 287 of mass then requires outward flow near the lower current collector, sinking
 288 near the center, and rising near the side walls. Arguments made with this
 289 poloidal circulation in mind lead to an expected scaling of electro-vortex flow
 290 as [61]

$$U_L \sim \frac{(\mu_0/\rho)^{1/2} I}{2\pi R}, \quad (18)$$

291 with μ_0 , I and R denoting the vacuum permeability, the cell current and
 292 radius, respectively. For other (but similar) possible scales, see [59, 60, 77,
 293 102].

294 In a flow in which both buoyant and electromagnetic forces are present,
 295 we expect flow speed to be predicted by (15) when buoyancy dominates and
 296 by (18) when electromagnetic forces dominate. We can moreover estimate
 297 which of the two effects dominates. The ratio of the characteristic velocities
 298 of electro-vortex flow to Rayleigh-Bénard convection is

$$A \sim \frac{(\mu_0/\rho)^{1/2} I}{2\pi R \sqrt{g\beta\Delta T h}} \quad (19)$$

299 and the ratio of the characteristic velocities of electro-vortex flow to internally

300 heated convection

$$B \sim \frac{R}{2h} \sqrt{\frac{\mu_o \sigma \lambda}{\rho g \beta h}}. \quad (20)$$

301 For alternative expressions, see [101, 103, 104]. We can think of equation
302 (19) as the ratio of momentum gained from electromagnetic forces to that
303 gained from buoyant forces in the core of the electrode, whereas equation
304 (20) can be thought of as the ratio of momentum gained by electromagnetic
305 forces to that dissipated by Joule heat. Hence, when $A \ll 1$ or $B \ll 1$, we
306 expect buoyancy to dominate the flow. When $A \gg 1$ and $B \gg 1$, we expect
307 electro-vortex flow to dominate.

308 The dimensionless ratios A and B are obtained from a simple formalistic
309 approach. Compared to the sophisticated considerations of Davidson et al.
310 for a similar problem [84], our approach is quite simplistic — probably too
311 simple. Most notably, our formulas do not cover the *distribution* of the
312 current density nor the diameter of the current collectors. These will — of
313 course — have a crucial influence on the flow magnitude, though they will not
314 change A and B . Nevertheless, we believe it is admissible to use A and B as
315 a first estimate for the relative importance of thermal convection and electro-
316 vortex flow. Table 1 shows both dimensionless quantities for our geometry for
317 eutectic PbBi as well as liquid sodium. Considering the low values of A , we
318 expect Rayleigh-Bénard convection to dominate in the experiment. This is
319 indeed the case, as we will show later. On the other hand, the dimensionless
320 quantity B is clearly larger than one. Thus, we expect electro-vortex flow
321 to dominate over internally heated convection. In experiments, however, the
322 unavoidable presence of classical Rayleigh-Bénard convection does not allow
323 comparing EVF and IHC directly.

324 Finally, a third dimensionless ratio can be used to estimate the transition
325 from poloidal electro-vortex to an azimuthal swirl flow. As its derivation is
326 effectively explained by Davidson et al. [61, 63], we give here only the result:
327 if an azimuthal force of a magnitude of 1 % of the poloidal one is present, we
328 expect swirl flow to dominate.

329 4. Results and discussion

330 In this section we present the measured and simulated velocities in the
331 liquid electrode without any current (Fig. 3), with $I = 2$ A (Fig. 4) and

Table 1: Dimensionless parameters for different electrode materials using the same geometry as in the experiment ($I = 40$ A, $R = 44.5$ mm, $h = 11$ mm, $\Delta T = 8$ K). For the material properties, see [91–93, 105, 106].

Component	A	B
Na anode	0.36	386
PbBi cathode	0.15	17.5

332 $I = 40$ A (Fig. 5). In all experiments, velocity profiles are recorded when the
 333 temperature of the vessel is stabilized at 160°C . The measured temperature
 334 difference between the top and bottom of the liquid metal was always in the
 335 range of $7\text{ K} \leq T - T_0 \leq 9\text{ K}$.

336 Figure 3a shows the measured radial velocity distribution along the di-
 337 ameter of the electrode recorded for two minutes. No current is applied; we
 338 observe only Rayleigh-Bénard convection. The flow is rather disordered. This
 339 fits well to the numerical results (Fig. 3c), obtained with no-slip boundary
 340 conditions for velocity, a fixed vertical temperature gradient and adiabatic
 341 side walls (The oxide film formed on the melt justifies using a no-slip bound-
 342 ary condition for the free surface [107]). Using the ultrasound beam model
 343 described in Appendix A we extract the radial velocity projection along the
 344 diameter of the UDV probe so that we can directly compare the mean ve-
 345 locity from experimental measurements with numerical simulations. Figure
 346 3b shows the mean velocity from experimental and numerical measurements
 347 (averaged over 100 s). Both agree fairly well with respect to the flow speed
 348 and the number of convection cells (illustrated in Fig. 3d). Though the flow
 349 is rather disordered, structure may be imposed via pinning of convection cells
 350 or heat transfer through the side walls. The top electrode certainly cools the
 351 metal bath in the middle. Such a finger cooling is well known to produce
 352 an axisymmetric flow in the Czochalski process of crystal growth [107, 108].
 353 Our configuration might also be compared to a flow driven by a localized
 354 (external) heat source [109–113].

355 When a (small) current $I = 2$ A is applied to the cell, the measured
 356 flow becomes immediately much more ordered (compare Fig. 3a and 4a); the
 357 measured flow magnitude does not change. Previous work dealing with liquid
 358 metal convection in the presence of magnetic fields suggest that convection
 359 rolls will tend to align with magnetic field lines, producing a more ordered
 360 flow structure [114, 115]. However, there are two other ways to explain the
 361 increase in order much better: electro-vortex flow and internally heated con-

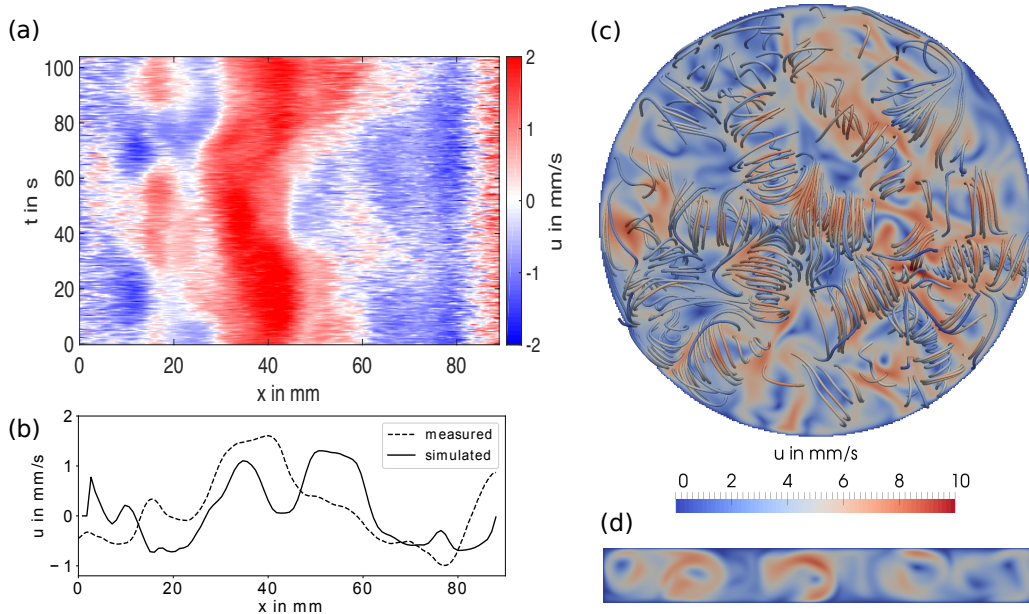


Figure 3: Pure Rayleigh-Bénard convection for $\Delta T = 8$ K. Measured radial velocity, (a). Mean speed across a diameter of the electrode, 6 mm above the vessel floor, (b), as measured (dashed curve) and simulated (solid curve). Speed and streamlines on a horizontal cross-section 5.5 mm above the vessel floor, (c). Speed on the vertical cross-section from which the ultrasound projection is extracted, (d). Rayleigh-Bénard convection drives disordered flow.

362 vection (IHC). Fig. 4e shows the simulated electro-vortex flow: a downward
 363 jet below the upper electrode, exactly as expected. In the same volume, most
 364 of the Joule heat will be generated. The strong radial temperature gradient
 365 forms lateral jets and several convection cells (Fig. 4d). Comparing Figs. 4d
 366 and e, three things are noteworthy: EVF and thermal convection have an
 367 opposing flow direction, the magnitude of the thermal flow is one order of
 368 magnitude larger than EVF, and both are fairly difficult to measure in our
 369 experiments. In vacuum arc remelting the same flow directions are observed.
 370 However, electro-vortex flow reaches — compared to thermal convection —
 371 a “similar size” [84] of e.g. 30% of the typical convection speed [101]. A
 372 direct comparison of the (time averaged) mean velocity projection along the
 373 diameter of the aforementioned flows is shown in Fig. 4b. The simulated flow
 374 profile for IHC matches the measurement well (black curves). However, the
 375 simulation shows velocities twice as large as the measured ones. We believe

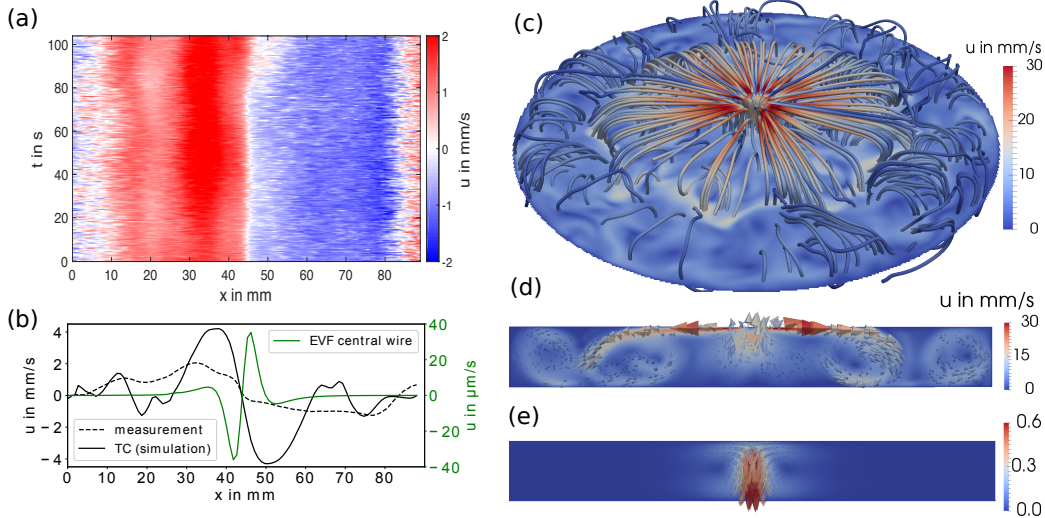


Figure 4: Convection and electro-vortex flow with $I = 2$ A. Measured radial velocity, (a). Mean speed across a diameter of the electrode, 6 mm above the vessel floor, (b), as measured (dashed curve) and simulated (solid curves). Speed and streamlines on a horizontal cross-section 5.5 mm above the vessel floor, (c). Flow due to internally heated convection (IHC) alone, on the vertical cross-section from which the ultrasound projection is extracted, (d). Flow due to electro-vortex flow (EVF) alone, on the same vertical cross-section, (e). IHC dominates EVF and has a shape consistent with experimental observations, but larger magnitude.

376 this discrepancy may be explained partially by the simplified boundary con-
 377 ditions (no-slip for velocity; fixed vertical temperature difference; adiabatic
 378 side-walls). Moreover, an interaction between the opposing EVF and ther-
 379 mal convection may change the flow structure, too. Despite the described
 380 challenges of measurement and simulation we can state: internally heated
 381 convection dominates the flow.

382 When I is increased to 40 A, the measured velocities increase by a factor
 383 of five (Fig. 5a). We no longer observe a global poloidal circulation, but a
 384 tornado-like flow structure emerges — a phenomenon well known from for-
 385 mer experiments [60, 74, 83]. Unfortunately, it is not possible to measure
 386 the azimuthal flow speed with our current experimental apparatus. Any-
 387 way, we know when swirl appears first: at 20 A, if the current is supplied
 388 symmetrically and at 10 A if is supplied from the side. As mentioned in the
 389 introduction, the *appearance* of azimuthal forces can easily be explained: the
 390 internal radial currents interact with a vertical stray magnetic field. This

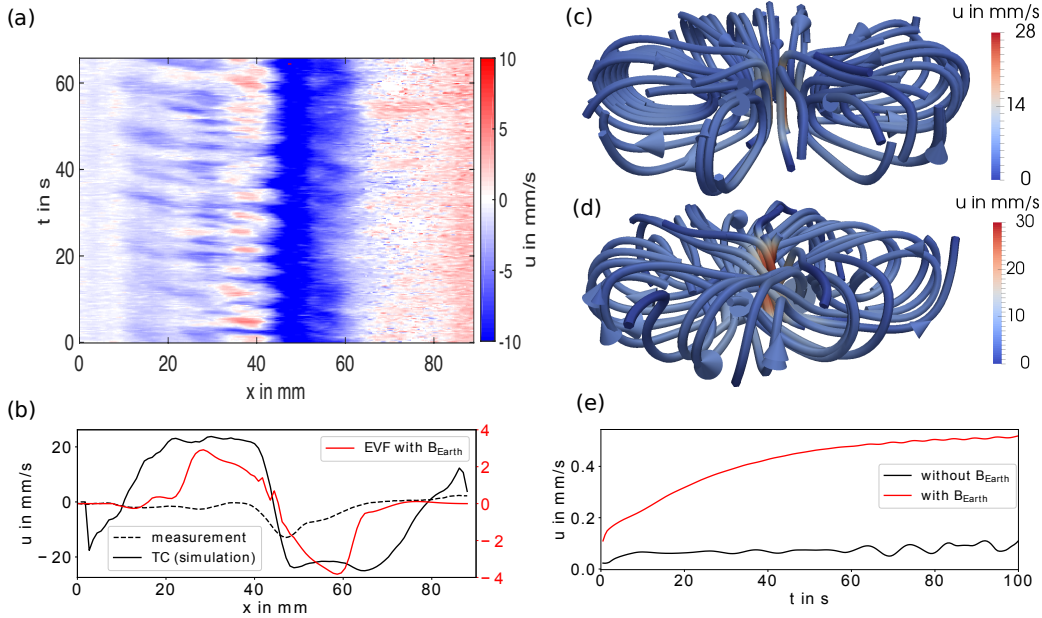


Figure 5: Convection and electro-vortex flow with $I = 40$ A. Measured radial velocity, (a). Mean speed across a diameter of the electrode, 6 mm above the vessel floor, (b), as measured (dashed curve) and simulated (solid curves). Streamlines of electro-vortex flow simulated without Earth’s magnetic field (c), and with it (d). Volumetrically-averaged poloidal and azimuthal velocity of electro-vortex flow (e). In (a) and (b), both internally heated convection and Rayleigh-Bénard convection are present. Earth’s field causes azimuthal flow in both experiments and simulations, but suppresses poloidal flow more strongly in experiments.

391 may be the Earth’s magnetic field of $B_z \approx 0.5$ mT or with the words of Bo-
 392 jarevics: the “slightest deviation from symmetry” leads to swirl [78], because
 393 it produces such fields [60, 61, 83]. The often observed *dominance* of the az-
 394 imuthal flow is harder to explain. While Millere assumes the kinetic energy
 395 of the poloidal flow to be “partially transferred to the rotational motion”
 396 [76], Shtern finds a supercritical bifurcation of the poloidal flow leading to
 397 swirl [86]. Davidson et al. point out that the model of the latter author is
 398 oversimplified. He explains the dominance of swirl as “poloidal suppression”
 399 [63], which is in the sense of [76] and [83]. Specifically, he describes that the
 400 swirling motion forces the poloidal flow into a thin, dissipative Ekman layer
 401 where it is suppressed efficiently.

402 In Figs. 5c and d we show the electro-vortex flow, simulated with and
 403 without the Earth’s magnetic field. The latter we measured in Dresden as

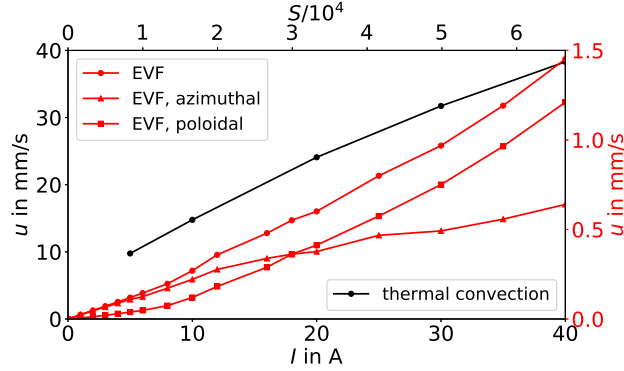


Figure 6: Volume-averaged velocity due to simulated internally heated convection (left axis) and electro-vortex flow (right axis). For these simulations we used symmetric current collectors and $\mathbf{B} = (15 \cdot \mathbf{e}_x, 5 \cdot \mathbf{e}_y, 36 \cdot \mathbf{e}_z) \mu\text{T}$. Though the speeds of both internal thermal convection and electro-vortex flow are predicted to scale linearly with current, we find that both deviate slightly.

404 $\mathbf{B} = (15 \cdot \mathbf{e}_x, 5 \cdot \mathbf{e}_y, 36 \cdot \mathbf{e}_z) \mu\text{T}$. Figure 5e illustrates, that indeed the azimuthal
 405 velocity increases due to the Earth’s magnetic field. In contrast to Davidson,
 406 we do not observe a strong poloidal suppression (compare with Fig. 9 in
 407 [63]); investigation of that discrepancy is underway. Finally, we compare
 408 measurement and simulation in Fig. 5b. Obviously, the profile of the flow
 409 matches well, while its magnitude does not. Simulating the effects of thermal
 410 convection and EVF separately is important, but it is not enough. Both
 411 phenomena interact: presumably the electromagnetically driven swirl flow
 412 suppresses the thermal flow as described by Davidson [63]. A more detailed
 413 experimental and numerical study of that interaction is planned for the near
 414 future.

415 A strong swirl flow may enhance mass transfer, but will also lead to
 416 differences in the centripetal pressure along the interface. If strong enough it
 417 will deform the electrode-electrolyte interface and may eventually lead to a
 418 short circuit of the cell [46, 116]. By this means, swirling electro-vortex flow
 419 could trigger interface instabilities in LMBs.

420 Figure 6 shows the simulated mean flow velocity of internally heated convection
 421 (left axis) and electro-vortex flow including the Earth’s magnetic field
 422 (right axis). As discussed before, thermal convection is one order of magni-
 423 tude larger than EVF. Though (15) predicts that thermal convection speed
 424 will increase linearly with current, we find the rate of increase to be slower.

425 On the other hand, the global EVF speed grows slightly faster than linearly
426 with current. According to Vlasyuk [59, 60] we would expect a quadratic
427 scaling up to $S = 1\,000$ and above $S = 10^5$ a linear scaling. Operating in the
428 transition region between both, our results seem to fit roughly to Vlasyuk's
429 theoretical prediction. Figure 6 also shows the poloidal and azimuthal mean
430 velocity of EVF. The poloidal mean velocity scales approximately quadrati-
431 cally with current, as one might expect. Increasing the cell current, we also
432 simultaneously increase the magnetic field induced by the current itself, with
433 which the current interacts to drive poloidal flow. The rather linear scaling
434 of the azimuthal flow can be explained in a very similar way. Here, only the
435 cell current — together with the *constant* vertical field of the Earth — drives
436 the flow.

437 5. Summary, design implications, and outlook

438 Using a combination of in-situ ultrasound velocity measurement and nu-
439 merical simulations, we studied the flow in a liquid PbBi electrode. Specif-
440 ically, we explored classical Rayleigh-Bénard convection, internally heated
441 convection (IHC), electro-vortex flow (EVF) and swirl flow. Using a steel
442 vessel and a point electrode (Fig. 2) we applied up to 40 A (0.65 A/cm^2).
443 We demonstrated that meaningful UDV measurements are possible in a thin
444 fluid layer of only 11 mm height. For the purpose of comparing experiment
445 and simulation, we developed a model for the ultrasound beam. Further,
446 we derived estimates of the relative importance of thermal convection and
447 electro-vortex flow, and pointed out the limitations of those estimates.

448 We found the velocity of internally heated convection to be one order of
449 magnitude larger than electro-vortex flow. This relates to our experiment
450 (with the point electrode); it might be different in a real liquid metal battery
451 (LMB). In our experiment, IHC and EVF drive flows of similar shape but in
452 opposing directions. At low current densities, we found thermal convection
453 to dominate the flow structure. The flow became more ordered with increas-
454 ing current. At higher currents we observed a strong interaction of all flow
455 phenomena. We found a good agreement of simulation and measurements for
456 low currents; as we modeled EVF and IHC separately (and did not account
457 for its interaction), experiment and simulation matched less closely at higher
458 currents. We found the mean velocity of EVF in typical LMBs (10 cm side
459 length) to be in order of mm/s.

460 We further observed (azimuthal) swirl flow experimentally at 20 A for a
461 symmetric experiment, or 10 A for an asymmetric experiment. The numerical
462 simulations confirmed that vertical magnetic stray fields can cause such flow.
463 However, they did not show a suppression of the (original) poloidal electro-
464 vortex flow by the swirling motion. This is not in line with the findings of [63],
465 probably due to the different geometries. These differences deserve further
466 examination. We found the velocity of thermal convection to increase less
467 than linearly with the current. We explained why swirling motion increases
468 approximately linearly and poloidal electro-vortex flow quadratically with
469 current.

470 The locations and topology of electrical connections affect all four of the
471 flow phenomena we have considered. The Joule heating that drives internally
472 heated convection is a consequence of electrical current, so the placement
473 and size of connections sets the IHC flow. Electro-vortex flow is driven by
474 interactions between the current in the battery and its own magnetic field,
475 both set by the connections with the electric circuit. Swirl flow is driven by
476 interactions between current in the battery and magnetic fields produced by
477 supply lines. And Joule heating of those supply lines can drive Rayleigh-
478 Bénard convection.

479 Battery designers might choose locations and topology of electrical con-
480 nections to promote mass transfer in the cathodes of liquid metal batter-
481 ies, thereby allowing faster cycling and preventing formation of intermetallic
482 phases. Rayleigh-Bénard convection may be a difficult phenomenon to use
483 for mixing, since batteries for grid-scale storage will likely be part of large ar-
484 rays, making it difficult to impose temperature differences at the boundaries.
485 Internally heated convection can produce good mixing, but nearly all Joule
486 heat in a liquid metal battery is produced in the electrolyte, located *above*
487 the cathode. The resulting stable temperature stratification tends to inhibit
488 internally heated convection, not drive it. Thus IHC may also be problematic
489 for designers. Electro-vortex flow seems more promising, because it can pro-
490 duce good mixing and because its magnitude can be adjusted by changing the
491 diameter of the current collector to cause more or less divergence of current.
492 Designers must understand, however, that they make a trade-off: reducing
493 current collector size to promote mixing by electro-vortex flow also increases
494 the resistance of the battery, reducing its voltage and efficiency. Also, real-
495 world electro-vortex flows would likely be less vigorous than the ones in our
496 experiments and simulations, which use a narrow current collector resulting
497 in extreme divergence of current. We expect swirl to be less effective at

498 promoting mass transfer than the other flow phenomena we have considered
499 because it drives primarily horizontal motion, but vertical mass transfer is
500 most helpful. We also expect swirl to deform the cathode-electrolyte inter-
501 face substantially in large batteries. For that reason, swirl flow will need
502 special attention as it will surely trigger interface instabilities. Designers
503 should route battery supply wires so as to minimize vertical magnetic fields.
504 Most importantly, the *interaction* of internally heated convection and
505 electro-vortex flow deserves further study. In addition, it will be important
506 to reveal how the flow speeds of all phenomena grow with larger currents in
507 larger cells. The appearance and growth of swirl deserves further numerical
508 investigation. In a real LMB cathode, EVF will drive a flow against a stable
509 temperature stratification. This configuration needs to be studied, as well.
510 Finally, flow speed measurements in a real 3-layer LMB would be a great
511 step forward.

512 Acknowledgments

513 This work was supported by the National Science Foundation under award
514 number CBET-1552182, by the Deutsche Forschungsgemeinschaft (DFG,
515 German Research Foundation) under award number 338560565 as well as the
516 Helmholtz-Gemeinschaft Deutscher Forschungszentren (HGF) in frame of the
517 Helmholtz Alliance “Liquid metal technologies” (LIMTECH). The computa-
518 tions were performed on the Bull HPC-Cluster “Taurus” at the Center for
519 Information Services and High Performance Computing (ZIH) at TU Dres-
520 den and on the cluster “Hydra” at Helmholtz-Zentrum Dresden-Rossendorf.
521 Fruitful discussions with A. Beltrán, V. Bojarevics, P. Davidson, S. Franke,
522 V. Galindo, G. Horstmann, J. Pal, J. Priede, D. Rübiger, F. Stefani, T. Vogt
523 and T. Wondrak on several aspects of electro-vortex flow and thermal con-
524 vection are gratefully acknowledged. N. Weber thanks Henrik Schulz for the
525 HPC support.

526 References

- 527 [1] S. Backhaus, M. Chertkov, Getting a grip on the electrical grid, *Physics*
528 *Today* 66 (5) (2013) 42–48. doi:10.1063/PT.3.1979.
- 529 [2] International Energy Agency (Ed.), *World Energy Outlook 2013*, In-
530 *ternational Energy Agency*, 2013.

- 531 [3] H. Kim, D. A. Boysen, J. M. Newhouse, B. L. Spatocco, B. Chung,
532 P. J. Burke, D. J. Bradwell, K. Jiang, A. A. Tomaszowska, K. Wang,
533 W. Wei, L. A. Ortiz, S. A. Barriga, S. M. Poizeau, D. R. Sadoway,
534 Liquid Metal Batteries: Past, Present, and Future, *Chemical Reviews*
535 113 (3) (2013) 2075–2099. doi:10.1021/cr300205k.
- 536 [4] K. Wang, K. Jiang, B. Chung, T. Ouchi, P. J. Burke, D. A.
537 Boysen, D. J. Bradwell, H. Kim, U. Muecke, D. R. Sadoway,
538 Lithium–antimony–lead liquid metal battery for grid-level energy stor-
539 age, *Nature* 514 (7522) (2014) 348–350. doi:10.1038/nature13700.
- 540 [5] H. Kim, D. A. Boysen, T. Ouchi, D. R. Sadoway, Calcium - bismuth
541 electrodes for large - scale energy storage, *Journal of Power Sources*
542 241 (2013) 239–248.
- 543 [6] T. Ouchi, H. Kim, B. L. Spatocco, D. R. Sadoway, Calcium-based
544 multi-element chemistry for grid-scale electrochemical energy storage,
545 *Nature Communications* 7 (2016) 10999. doi:10.1038/ncomms10999.
- 546 [7] S. Poizeau, H. Kim, J. M. Newhouse, B. L. Spatocco, D. R. Sadoway,
547 Determination and modeling of the thermodynamic properties of liquid
548 calcium–antimony alloys, *Electrochimica Acta* 76 (2012) 8–15. doi:
549 10.1016/j.electacta.2012.04.139.
- 550 [8] T. Ouchi, H. Kim, X. Ning, D. R. Sadoway, Calcium-Antimony Alloys
551 as Electrodes for Liquid Metal Batteries, *Journal of The Electrochem-
552 ical Society* 161 (12) (2014) A1898–A1904.
- 553 [9] B. Agruss, H. R. Karas, The Thermally Regenerative Liquid Metal
554 Concentration Cell, in: R. F. Gold (Ed.), *Regenerative EMF Cells*,
555 Vol. 64 of *Advances in Chemistry*, American Chemical Society, Wash-
556 ington, D.C., 1967, pp. 62–81.
- 557 [10] M. S. Foster, S. E. Wood, C. E. Crouthamel, Thermodynamics of
558 Binary Alloys. I. The Lithium-Bismuth System, *Inorg. Chem.* 3 (10)
559 (1964) 1428 – 1431.
- 560 [11] X. Ning, S. Phadke, B. Chung, H. Yin, P. Burke, D. R. Sadoway, Self-
561 healing Li–Bi liquid metal battery for grid-scale energy storage, *Jour-
562 nal of Power Sources* 275 (2015) 370–376. doi:10.1016/j.jpowsour.
563 2014.10.173.

- 564 [12] E. J. Cairns, C. E. Crouthamel, A. K. Fischer, M. S. Foster, J. C. Hesson,
565 C. E. Johnson, H. Shimotake, A. D. Tevebaugh, Galvanic Cells
566 with Fused-Salt Electrolytes, ANL-7316, Argonne National Laboratory,
567 1967.
- 568 [13] E. J. Cairns, H. Shimotake, High-Temperature Batteries, *Science* 164
569 (1969) 1347–1355.
- 570 [14] E. J. Cairns, H. Shimotake, Recent advances in fuel cells and their
571 application to new hybrid systems, *Advances in Chemistry* 90 (1969)
572 321–350.
- 573 [15] M. S. Foster, C. E. Crouthamel, S. E. Wood, Thermodynamics of Bi-
574 nary Alloys. II. The Lithium-Tin System, *J. Phys. Chem.* 70 (10) (1966)
575 3042 – 3045.
- 576 [16] J. C. Hesson, H. Shimotake, Thermodynamics and thermal efficiencies
577 of thermally regenerative bimetallic and hydride emf cell systems, in:
578 Regenerative EMF Cells, American Chemical Society, 1967, pp. 82–
579 104.
- 580 [17] H. Shimotake, G. L. Rogers, E. J. Cairns, Secondary Cells with Lithium
581 Anodes and Immobilized Fused-Salt Electrolytes, *Industrial & Engi-
582 neering Chemistry Process Design and Development* 8 (1) (1969) 51–
583 56.
- 584 [18] D. J. Bradwell, H. Kim, A. H. C. Sirk, D. R. Sadoway, Magnesium–Antimony
585 Liquid Metal Battery for Stationary Energy Storage, *Journal of the American
586 Chemical Society* 134 (4) (2012) 1895–1897.
587 doi:10.1021/ja209759s.
- 588 [19] H. Shimotake, E. J. Cairns, Bimetallic galvanic cells with fused-salt
589 electrolytes, in: *Advances in Energy Conversion Engineering*, ASME,
590 Florida, 1967, pp. 951–962.
- 591 [20] M. S. Foster, G. H. McCloud, E. J. Cairns, Electrochemical studies of
592 the Sodium-Bismuth system, *Amer. Chem Soc.* (1967) 276 – 281.
- 593 [21] L. A. Herédy, M. L. Iverson, G. D. Ulrich, H. L. Recht, Development
594 of a thermally regenerative Sodium-Mercury galvanic system Part I
595 Electrochemical and Chemical Behavior of Sodium-Mercury Galvanic

- 596 Cells, in: Regenerative EMF Cells, American Chemical Society, 1967,
597 pp. 30–42.
- 598 [22] B. L. Spatocco, P. J. Burke, D. R. Sadoway, Low temperature liq-
599 uid metal batteries for grid-scaled storage, US patent no. 0099522 A1
600 (2014).
- 601 [23] R. D. Weaver, S. W. Smith, N. L. Willmann, The Sodium-Tin Liquid-
602 Metal Cell, *Journal of The Electrochemical Society* 109 (8) (1962) 653–
603 657.
- 604 [24] B. Agruss, The Thermally Regenerative Liquid-Metal Cell, *Journal of*
605 *The Electrochemical Society* 110 (11) (1963) 1097–1103.
- 606 [25] J. Xu, O. S. Kjos, K. S. Osen, A. M. Martinez, O. E. Kongstein, G. M.
607 Haarberg, Na-Zn liquid metal battery, *Journal of Power Sources* 332
608 (2016) 274–280. doi:10.1016/j.jpowsour.2016.09.125.
- 609 [26] J. Xu, A. M. Martinez, K. S. Osen, O. S. Kjos, O. E. Kongstein, G. M.
610 Haarberg, Electrode Behaviors of Na-Zn Liquid Metal Battery, *Journal*
611 *of The Electrochemical Society* 164 (12) (2017) A2335–A2340.
- 612 [27] N. E. Holubowitch, S. E. Manek, J. Landon, C. A. Lippert, S. A. Odom,
613 K. Liu, Cathode candidates for zinc-based thermal-electrochemical en-
614 ergy storage: Cathodes for Zn-based thermal-electrochemical energy
615 storage, *International Journal of Energy Research* 40 (3) (2016) 393–
616 399. doi:10.1002/er.3385.
617 URL <http://doi.wiley.com/10.1002/er.3385>
- 618 [28] N. E. Holubowitch, S. E. Manek, J. Landon, C. A. Lippert, S. A.
619 Odom, K. Liu, Molten Zinc Alloys for Lower Temperature, Lower Cost
620 Liquid Metal Batteries, *Advanced Materials Technologies* 1 (3) (2016)
621 1600035. doi:10.1002/admt.201600035.
- 622 [29] D. A. J. Swinkels, Molten Salt Batteries and Fuel Cells, in: J. Braun-
623 stein, G. Mamantov, G. P. Smith (Eds.), *Advances in Molten Salt*
624 *Chemistry*, Vol. 1, Plenum Press, New York, 1971, pp. 165–223.
- 625 [30] M. S. Foster, Laboratory Studies of Intermetallic Cells, in: Regenera-
626 tive EMF Cells, American Chemical Society, 1967, pp. 136–148.

- 627 [31] R. C. Vogel, M. Levenson, E. R. Proud, J. Royal, Chemical engineering
628 division research highlights, Tech. Rep. ANL-7350, Argonne National
629 Laboratory (1967).
- 630 [32] J. A. Shercliff, Fluid motions due to an electric current source, *J. Fluid*
631 *Mech.* 40 (1970) 241–250.
- 632 [33] F. Stefani, T. Weier, T. Gundrum, G. Gerbeth, How to circumvent the
633 size limitation of liquid metal batteries due to the Tayler instability,
634 *Energy Conversion and Management* 52 (2011) 2982–2986.
- 635 [34] M. Seilmayer, F. Stefani, T. Gundrum, T. Weier, G. Gerbeth,
636 M. Gellert, G. Rüdiger, Experimental Evidence for a Transient Tayler
637 Instability in a Cylindrical Liquid-Metal Column, *Phys. Rev. Lett.*
638 108 (244501).
- 639 [35] N. Weber, V. Galindo, F. Stefani, T. Weier, T. Wondrak, Numerical
640 simulation of the Tayler instability in liquid metals, *New Journal of*
641 *Physics* 15 (043034).
- 642 [36] N. Weber, V. Galindo, F. Stefani, T. Weier, Current-driven flow in-
643 stabilities in large-scale liquid metal batteries, and how to tame them,
644 *Journal of Power Sources* 265 (2014) 166–173.
- 645 [37] W. Herreman, C. Nore, L. Cappanera, J.-L. Guermond, Tayler insta-
646 bility in liquid metal columns and liquid metal batteries, *Journal of*
647 *Fluid Mechanics* 771 (2015) 79–114. doi:10.1017/jfm.2015.159.
- 648 [38] M. Starace, N. Weber, M. Seilmayer, T. Weier, F. Stefani, S. Eckert,
649 Ultrasound Doppler flow measurements in a liquid metal column under
650 the influence of a strong axial electric current, *Magnetohydrodynamics*
651 51 (2015) 249–256.
- 652 [39] N. Weber, V. Galindo, F. Stefani, T. Weier, The Tayler instability
653 at low magnetic Prandtl numbers: Between chiral symmetry breaking
654 and helicity oscillations, *New Journal of Physics* 17 (11) (2015) 113013.
655 doi:10.1088/1367-2630/17/11/113013.
- 656 [40] T. Weier, A. Bund, W. El-Mofid, G. M. Horstmann, C.-C. Lalau,
657 S. Landgraf, M. Nimtz, M. Starace, F. Stefani, N. Weber, Liquid

- 658 metal batteries - materials selection and fluid dynamics, IOP Conf.
659 Ser.: Mater. Sci. Eng. 228 (012013).
- 660 [41] T. Sele, Instabilities of the metal surface in electrolytic alumina re-
661 duction cells, Metallurgical and Materials Transactions B 8 (4) (1977)
662 613–618.
- 663 [42] O. Zikanov, Metal pad instabilities in liquid metal batteries, Physical
664 Review E 92 (063021).
- 665 [43] N. Weber, P. Beckstein, V. Galindo, W. Herreman, C. Nore, F. Stefani,
666 T. Weier, Metal pad roll instability in liquid metal batteries, Magne-
667 tohydrodynamics 53 (1) (2017) 129–140.
- 668 [44] N. Weber, P. Beckstein, W. Herreman, G. M. Horstmann, C. Nore,
669 F. Stefani, T. Weier, Sloshing instability and electrolyte layer rupture
670 in liquid metal batteries, Physics of Fluids 29 (5) (2017) 054101. doi:
671 10.1063/1.4982900.
- 672 [45] V. Bojarevics, A. Tucs, MHD of Large Scale Liquid Metal Batteries,
673 in: A. P. Ratvik (Ed.), Light Metals 2017, Springer International Pub-
674 lishing, Cham, 2017, pp. 687–692.
- 675 [46] G. M. Horstmann, N. Weber, T. Weier, Coupling and stability of in-
676 terfacial waves in liquid metal batteries, arXiv:1708.02159.
- 677 [47] O. Zikanov, Shallow water modeling of rolling pad instability in liquid
678 metal batteries, arXiv:1706.08589.
- 679 [48] Y. Shen, O. Zikanov, Thermal convection in a liquid metal battery,
680 Theoretical and Computational Fluid Dynamics 30 (4) (2016) 275–294.
681 doi:10.1007/s00162-015-0378-1.
- 682 [49] T. Köllner, T. Boeck, J. Schumacher, Thermal Rayleigh-Marangoni
683 convection in a three-layer liquid-metal-battery model, Physical Review
684 E 95 (053114). doi:10.1103/PhysRevE.95.053114.
- 685 [50] D. H. Kelley, D. R. Sadoway, Mixing in a liquid metal electrode, Physics
686 of Fluids 26 (5) (2014) 057102. doi:10.1063/1.4875815.

- 687 [51] A. Beltrán, MHD natural convection flow in a liquid metal electrode,
688 Applied Thermal Engineering 114 (2016) 1203–1212. doi:10.1016/j.
689 applthermaleng.2016.09.006.
- 690 [52] W. Wang, K. Wang, Simulation of thermal properties of the liq-
691 uid metal batteries, in: Power Electronics Systems and Applications
692 (PESA), 2015 6th International Conference On, IEEE, 2015, pp. 1–11.
- 693 [53] D. Bradwell, G. Ceder, L. A. Ortiz, D. R. Sadoway, Liquid electrode
694 battery, US patent no. US 2011/0014505 A1.
- 695 [54] D. Bradwell, G. Ceder, L. A. Ortiz, D. R. Sadoway, Liquid metal alloy
696 energy storage device, US patent no. US 9,076,996 B2 (2015).
- 697 [55] N. Weber, V. Galindo, J. Priede, F. Stefani, T. Weier, The influence
698 of current collectors on Tayler instability and electro vortex flows in
699 liquid metal batteries, Physics of Fluids 27 (014103).
- 700 [56] S. Lundquist, On the hydromagnetic viscous flow generated by a di-
701 verging electric current, Arkiv fr Fysik 40 (5) (1969) 89–95.
- 702 [57] E. V. Shcherbinin, Electrically conducting fluid in self magnetic field
703 of an electric current, Magnetohydrodynamics 11 (1) (1975) 68–74.
- 704 [58] C. Sozou, On fluid motions induced by an electric current source, J.
705 Fluid Mech. 46 (1971) 25–32.
- 706 [59] V. K. Vlasyuk, Effects of fusible-electrode radius on the electrovortex
707 flow in a cylindrical vessel, Magnitnaya Gidrodinamika 4 (1987) 101–
708 106.
- 709 [60] V. Bojarevičs, Y. Freibergs, E. I. Shilova, E. V. Shcherbinin, Electrically
710 Induced Vortical Flows, Kluwer Academic Publishers, 1989.
- 711 [61] P. A. Davidson, An Introduction to Magnetohydrodynamics, Cam-
712 bridge texts in applied mathematics, Cambridge University Press,
713 Cambridge ; New York, 2001.
- 714 [62] V. Shatrov, G. Gerbeth, Stability of the electrically induced flow be-
715 tween two hemispherical electrodes, Magnetohydrodynamics 48 (3).

- 716 [63] P. A. Davidson, D. Kinnear, R. J. Lingwood, D. J. Short, X. He, The
717 role of Ekman pumping and the dominance of swirl in confined flows
718 driven by Lorentz forces, *Eur. J. Mech. B* 18 (1999) 693–711.
- 719 [64] L. A. Volokhonskii, Dynamic boundary layer of electrovortex flow in a
720 cylindrical volume with axisymmetric current supply, *Magnetohydro-*
721 *dynamics* 27 (4) (1991) 467–470.
- 722 [65] V. N. Zhigulev, Some Magneto-Fluid Dynamic Effects in a Finitely
723 Conducting Medium, *Reviews of Modern Physics* 32 (4) (1960) 828.
- 724 [66] V. N. Zhigulev, The phenomenon of ejection by an electrical discharge,
725 *Doklady Akademii Nauk SSSR* 130 (2) (1960) 280–283.
- 726 [67] C. Sozou, H. English, Fluid motion induced by an electric current dis-
727 charge, *Proc. R. Soc. Lond. A.* 329 (1972) 71–81.
- 728 [68] C. Sozou, Fluid motions induced by an electric current jet, *Physics of*
729 *Fluids* 15 (2) (1972) 272. doi:10.1063/1.1693904.
- 730 [69] J. P. Narain, Fluid motion caused by conical currents, *Physics of Fluids*
731 16 (6) (1973) 940. doi:10.1063/1.1694451.
- 732 [70] A. J. M. Jansen, Fluid motions generated by the injection of an electric
733 current, Ph.D. thesis, TU Delft (1986).
- 734 [71] A. A. Petrunin, V. N. Shtern, Bifurcation of poloidal field in the flow in-
735 duced by a radial electric current, *Izvestiya Rossiiskoi Akademii Nauk,*
736 *Mekhanika Zhidkosti i Gaza* 2 (1993) 4–11.
- 737 [72] H. K. Moffatt, Some problems in the magnetohydrodynamics of liquid
738 metals, *Gesellschaft angewandte Mathematik und Mechanik Jahrestag-*
739 *ung Goettingen West Germany Zeitschrift Flugwissenschaften* 58.
- 740 [73] A. Y. Chudnovskii, Modeling electrovortex flows, *Magnetohydrody-*
741 *namics* 25 (3) (1989) 337–341.
- 742 [74] R. A. Woods, D. R. Milner, Motion in the weld pool in arc welding,
743 *Welding Journal* 50 (1971) 163–173.

- 744 [75] I. E. Butsenieks, D. E. Peterson, V. I. Sharamkin, E. V. Sherbinin,
745 Magnetohydrodynamic fluid flows in a closed space with a nonuniform
746 electric current, *Magnitnaya Gidrodinamika* 1 (1976) 92–97.
- 747 [76] R. P. Millere, V. I. Sharamkin, E. V. Shcherbinin, Effect of a longitudi-
748 nal magnetic field on electrically driven rotational flow in a cylindrical
749 vessel, *Magnitnaya Gidrodinamika* 1 (1980) 81–85.
- 750 [77] A. Y. Chudnovskii, Evaluating the intensity of a single class of electro-
751 vortex flows MHD, *Magnetohydrodynamics* 25 (3) (1989) 406–408.
- 752 [78] V. V. Boyarevich, V. I. Sharamkin, MHD flows due to current spreading
753 in an axisymmetric layer of finite thickness, *Magnitnaya Gidrodinamika*
754 2 (1977) 55–60.
- 755 [79] V. G. Zhilin, Y. P. Ivochkin, A. A. Oksman, G. R. Lurin'sh, A. I.
756 Chaikovskii, A. Y. Chudnovskii, E. V. Shcherbinin, An experimental
757 investigation of the velocity field in an axisymmetric electrovortical
758 flow in a cylindrical container, *Magnitnaya Gidrodinamika* 3 (1986)
759 110–116.
- 760 [80] D. Rübiger, Y. Zhang, V. Galindo, S. Franke, B. Willers, S. Eckert, The
761 relevance of melt convection to grain refinement in Al–Si alloys solid-
762 ified under the impact of electric currents, *Acta Materialia* 79 (2014)
763 327–338. doi:10.1016/j.actamat.2014.07.037.
- 764 [81] Y. H. Zhang, D. Rübiger, S. Eckert, Solidification of pure aluminium af-
765 fected by a pulsed electrical field and electromagnetic stirring, *J. Mater.*
766 *Sci.* 51 (4) (2016) 2153–2159. doi:10.1007/s10853-015-9525-8.
- 767 [82] S. Franke, D. Rübiger, V. Galindo, Y. Zhang, S. Eckert, Investi-
768 gations of electrically driven liquid metal flows using an ultrasound
769 Doppler flow mapping system, *Flow Measurement and Instrumenta-*
770 *tion* 48 (2016) 64–73. doi:10.1016/j.flowmeasinst.2015.09.004.
- 771 [83] V. Bojarevics, E. V. Shcherbinin, Azimuthal rotation in the axisym-
772 metric meridional flow due to an electric-current source, *Journal of*
773 *Fluid Mechanics* 126 (1983) 413. doi:10.1017/S0022112083000245.

- 774 [84] P. A. Davidson, Overcoming instabilities in aluminium reduction cells:
775 A route to cheaper aluminium, *Materials Science and Technology* 16 (5)
776 (2000) 475–479.
- 777 [85] H. Schlichting, K. Gersten, E. Krause, H. Schlichting, H. Schlichting,
778 *Grenzschicht-Theorie*, Springer, Berlin, 2006, oCLC: 636610285.
- 779 [86] V. Shtern, A. Barrero, Bifurcation of swirl in liquid cones, *Journal of*
780 *Fluid Mechanics* 300 (1995) 169. doi:10.1017/S002211209500365X.
- 781 [87] R. F. Ashour, H. Yin, T. Ouchi, D. H. Kelley, D. R. Sadoway,
782 *Communication Molten Amide-Hydroxide-Iodide Electrolyte for a Low-*
783 *Temperature Sodium-Based Liquid Metal Battery*, *Journal of The*
784 *Electrochemical Society* 164 (2) (2017) A535–A537. doi:10.1149/2.
785 1451702jes.
- 786 [88] A. Perez, D. H. Kelley, Ultrasound Velocity Measurement in a Liquid
787 Metal Electrode, *Journal of Visualized Experiments* 102 (e52622). doi:
788 10.3791/52622.
- 789 [89] I. Kolesnichenko, S. Khripchenko, D. Buchenau, G. Gerbeth, Electro-
790 vortex flows in a square layer of liquid metal, *Magnetohydrodynamics*
791 41 (2005) 39–51.
- 792 [90] H. G. Weller, G. Tabor, H. Jasak, C. Fureby, A tensorial approach to
793 computational continuum mechanics using object-oriented techniques,
794 *Comput. Phys.* 12 (6) (1998) 620–631.
- 795 [91] V. Sobolev, Thermophysical properties of lead and lead–bismuth eu-
796 tectic, *Journal of Nuclear Materials* 362 (2-3) (2007) 235–247. doi:
797 10.1016/j.jnucmat.2007.01.144.
- 798 [92] V. Sobolev, Database of Thermophysical Properties of Liquid Metal
799 Coolants for GEN-IV, SCK CEN, 2010.
- 800 [93] Nuclear Energy Agency, Handbook on Lead-bismuth Eutectic Alloy
801 and Lead Properties, Materials Compatibility, Thermalhydraulics and
802 Technologies, Tech. Rep. 7268, Nuclear Energy Agency (2015).
- 803 [94] A. Oberbeck, Über die Wärmeleitung der Flüssigkeiten bei der
804 Berücksichtigung der Strömungen infolge von Temperaturdifferenzen,
805 *Ann. Phys.* 7 (271).

- 806 [95] D. D. Gray, A. Giorgini, The validity of the Boussinesq approximation
807 for liquids and gases, *Int. J. Heat Mass Transfer* 19 (1976) 545–551.
- 808 [96] S. Zhang, X. Zhao, General Formulations for Rhie-Chow Interpolation,
809 in: *ASME 2004 Heat Transfer/Fluids Engineering Summer Conference*,
810 2004, pp. 567–573.
- 811 [97] N. Weber, P. Beckstein, V. Galindo, M. Starace, T. Weier,
812 Electro-vortex flow simulation using coupled meshes, arXiv preprint
813 arXiv:1707.06546.
- 814 [98] P. K. Kundu, I. M. Cohen, D. R. Dowling, *Fluid Mechanics*, Academic
815 Press, 2012.
- 816 [99] N. Shi, M. S. Emran, J. Schumacher, Boundary layer structure in tur-
817 bulent Rayleigh–Bénard convection, *J. Fluid Mech.* 706 (2012) 5–33.
818 doi:10.1017/jfm.2012.207.
- 819 [100] D. Goluskin, Internally heated convection beneath a poor conductor,
820 *J. Fluid Mech.* 771 (2015) 36–56. doi:10.1017/jfm.2015.140.
- 821 [101] O. Kazak, Modeling of Vortex Flows in Direct Current (DC) Electric
822 Arc Furnace with Different Bottom Electrode Positions, *Metallurgical
823 and Materials Transactions B* 44 (5) (2013) 1243–1250. doi:10.1007/
824 s11663-013-9899-4.
- 825 [102] O. V. Kazak, A. N. Semko, Numerical modeling of electro-vortical flows
826 in a confined volume, *J. Eng. Phys. Thermophys.* 85 (2012) 1167–1178.
- 827 [103] D. R. Atthey, A mathematical model for fluid flow in a weld pool at
828 high currents, *Journal of Fluid Mechanics* 98 (4) (1980) 787–801.
- 829 [104] P. A. Nikrityuk, K. Eckert, R. Grundmann, Y. S. Yang, An Impact
830 of a Low Voltage Steady Electrical Current on the Solidification of a
831 Binary Metal Alloy: A Numerical Study, *steel research international*
832 78 (5) (2007) 402–408.
- 833 [105] International Atomic Energy Agency, *Thermophysical Properties of*
834 *Materials for Nuclear Engineering: A Tutorial and Collection of Data.*,
835 International Atomic Energy Agency, Vienna, 2008.

- 836 [106] C. J. Smithells, W. F. Gale, T. C. Totemeier, *Smithells Metals Refer-*
837 *ence Book*, 8th Edition, Elsevier Butterworth-Heinemann, Amsterdam
838 ; Boston, 2004.
- 839 [107] A. Cramer, J. Pal, G. Gerbeth, Ultrasonic flow measurements in a
840 model of a Czochralski puller, *Flow Meas. Instrum.* 37 (2014) 99–106.
841 doi:10.1016/j.flowmeasinst.2014.03.008.
- 842 [108] J. Pal, A. Cramer, I. Grants, S. Eckert, G. Gerbeth, Physical mod-
843 elling of temperature fluctuations in a high aspect ratio model of
844 the Czochralski crystal growth, *J. Cryst. Growth* 432 (2015) 69–77.
845 doi:10.1016/j.jcrysgr.2015.09.009.
- 846 [109] J. M. Lopez, F. Marques, Instability of plumes driven by localized
847 heating, *Journal of Fluid Mechanics* 736 (2013) 616–640. doi:10.
848 1017/jfm.2013.537.
- 849 [110] M. C. Navarro, A. M. Mancho, H. Herrero, Instabilities due to a heating
850 spike, *Journal of Physics: Conference Series* 64 (2007) 012003. doi:
851 10.1088/1742-6596/64/1/012003.
- 852 [111] M. C. Navarro, A. M. Mancho, H. Herrero, Instabilities in buoyant
853 flows under localized heating, *Chaos: An Interdisciplinary Journal of*
854 *Nonlinear Science* 17 (2) (2007) 023105. doi:10.1063/1.2714295.
- 855 [112] M. C. Navarro, H. Herrero, Vortices in a cylindrical annulus nonhomo-
856 geneously heated: Effect of localized heating on their stability and in-
857 tensity, *Physical Review E* 84 (3). doi:10.1103/PhysRevE.84.037301.
- 858 [113] M. C. Navarro, H. Herrero, Top-down vortices developed in a cylin-
859 drical annulus cooled on the top, *Physical Review E* 88 (1). doi:
860 10.1103/PhysRevE.88.015002.
- 861 [114] U. Burr, U. Müller, Rayleigh–Bénard convection in liquid metal layers
862 under the influence of a horizontal magnetic field, *Journal of Fluid*
863 *Mechanics* 453 (2002) 345–369.
- 864 [115] Y. Tasaka, K. Igaki, T. Yanagisawa, T. Vogt, T. Zuerner, S. Eck-
865 ert, Regular flow reversals in Rayleigh–Bénard convection in a horizon-
866 tal magnetic field, *Phys. Rev. E* 93 (4). doi:10.1103/PhysRevE.93.
867 043109.

- 868 [116] D. Munger, A. Vincent, A cylindrical model for rotational MHD
869 instabilities in aluminum reduction cells, *Theoretical and Compu-*
870 *tational Fluid Dynamics* 22 (5) (2008) 363–382. doi:10.1007/
871 s00162-008-0082-5.
- 872 [117] J. Krautkrämer, H. Krautkrämer, *Werkstoffprüfung mit Ultraschall*,
873 Springer-Verlag, 1986.
- 874 [118] Signal Processing S.A., DOP3000 series User’s manual.

875 **Appendix A. Effect of acoustic beam broadening on UDV mea-**
876 **surements**

877 In order to precisely compare experimental results gained from UDV mea-
878 surements to numerical simulations, it is necessary to account for the fact
879 that each ultrasound pulse broadens spatially as it travels away from the
880 emitting transducer, thereby reducing the lateral resolution with increasing
881 distance. Therefore, the measured velocity at each distance interval will be a
882 weighted average over the radial fluid velocity component (pointing toward
883 or away from the transducer) within the width of the beam at that distance
884 interval.

885 The pressure waves generated by a flat, circular transducer can be thought
886 of the product of many adjacent point sources in accordance with the Huygens-
887 Fresnel principle. As a result, the ultrasound field in the region near the
888 transducer has a complicated structure. The distance z along the axis of the
889 transducer and the intensity I_z follow the relation

$$I_z = I_0 \sin^2 \left(\frac{\pi}{\lambda} \left(\sqrt{r_T^2 + z^2} - z \right) \right) \quad (\text{A.1})$$

890 rather than the inverse square law followed by the intensity of spherical
891 waves [117]. Here, I_0 is the maximum intensity, λ is the wavelength, and
892 r_T the radius of the transducer. Along the transducer axis, intensity maxima
893 occur when

$$\frac{\pi}{\lambda} \left(\sqrt{r_T^2 + z^2} - z \right) = \left(\frac{1}{2} + n \right) \pi; n \in \mathbb{N}_0. \quad (\text{A.2})$$

894 The axial distances of these maxima are then

$$z = \frac{r_T^2 - \left(\frac{1}{2} + n\right)^2 \lambda^2}{2 \left(\frac{1}{2} + n\right) \lambda}. \quad (\text{A.3})$$

895 The furthest peak of this function occurs when $n = 0$ at distance

$$z_{nf} = \frac{r_T^2 - \left(\frac{1}{4}\right) \lambda^2}{\lambda}. \quad (\text{A.4})$$

896 This is the boundary of the near field, or Fresnel zone, beyond which lies
 897 the far field, or Fraunhofer zone. In the Fresnel zone, the acoustic field can be
 898 approximated as retaining the same cross section as the transducer [118]. In
 899 the Fraunhofer zone, the intensity decreases continuously (converging toward
 900 the inverse square law at infinity). Moreover, the ultrasound field spreads out
 901 conically. This can be quantified by the directivity function of the pressure
 902 wave $D(\theta)$, which weighs the acoustic intensity with respect to the angle θ
 903 off the transducer axis

$$D(\theta) = \frac{2J_1(kr_T \sin \theta)}{kr_T \sin \theta}, \quad (\text{A.5})$$

904 where J_1 is the Bessel function of the first kind and first order and $k = \frac{2\pi}{\lambda}$ is
 905 the wavenumber [117]. The intensity as a function of the z coordinate and
 906 angle is then

$$\frac{I(z, \theta)}{I_0} = \sin^2 \left(\frac{\pi}{\lambda} \left(\sqrt{r_T^2 + z^2} - z \right) \right) (D(\theta))^2. \quad (\text{A.6})$$

907 The angle of divergence is where the intensity's first root lies [117, 118]:

$$\theta_0 = \arcsin \left(\frac{0.61\lambda}{r_T} \right). \quad (\text{A.7})$$

908 $I(z, \theta)/I_0$ is used as a weighting factor when averaging over the radial
 909 velocity components of each point within θ_0 at a certain distance from the
 910 transducer in the numerical model. This is done to compare it to experimen-
 911 tal results. The weighting factor and beam broadening (green planes) are
 912 illustrated in Fig. 2.